The Sherman function in highly relativistic elastic electron–atom scattering

The Sherman function in highly relativistic elastic electron–atom scattering

D H Jakubassa-Amundsen[1] and R Barday[2,3]

[1] Mathematisches Institut, Universität München, Theresienstraße 39, 80333 Munich, Germany
[2] Institut für Kernphysik, Technische Universität Darmstadt, Schlossgartenstraße 9, 64289 Darmstadt, Germany
[3] Helmholtz-Zentrum Berlin, Albert-Einstein-Straße 15, 12489 Berlin, Germany

E-mail: dj@math.lmu.de

Abstract

The Sherman function, which is a measure of the spin asymmetry in the elastic scattering of transversely polarized electrons from heavy targets, is calculated within the relativistic partial-wave representation. For collision energies above 40 MeV, oscillations of the Sherman function develop at the backward scattering angles which mirror the influence of the nuclear potential and which scale inversely with the nuclear size. We give predictions for 20–200 MeV electrons colliding with ^{64}Zn, ^{208}Pb and ^{238}U. We propose the measurement of the diffraction structures in the angular distribution of the Sherman function for a ^{208}Pb target at a beam energy near 80 MeV. The feasibility of such an experiment is addressed.

(Some figures may appear in colour only in the online journal)

1. Introduction

The theoretical prediction of polarization effects in elastic electron scattering dates back to Mott [1, 2]. The first unambiguous detection of a polarization asymmetry [3] was interpreted as confirmation of the relativistic Dirac theory. In the case of spin-polarized electron beams, a scattering asymmetry occurs when the orientation of the beam polarization with respect to the scattering plane is flipped. The Sherman function S, also termed 'analyzing power', is a measure of this spin asymmetry and was originally evaluated by Sherman [4] with the help of a partial-wave expansion of the relativistic scattering amplitude [5]. Apart from characterizing the asymmetry in the case of a polarized electron beam, the Sherman function also provides a measure of the polarization of the scattered electrons when the beam is unpolarized. In the traditional double-scattering experiments with unpolarized beams, both properties of S can be combined [3, 6–8].

While there is a considerable amount of literature on such low-energy scattering (well below 1 MeV where, e.g., screening effects play a dominant role, see the reviews by Motz

et al [6] and Kessler [9]), we shall focus on much higher collision energies. There exist a few pilot measurements of the Sherman function between 1 and 14 MeV, using polarized electron beams [10, 11]. At energies near 15 MeV and above, nuclear physics effects come into play. The most important of these is the influence of the finite nuclear size when the de Broglie wavelength of the electron falls below the nuclear radius. Nuclear size effects in the Sherman function were first taken into account in [12, 13] within the framework of the second Born approximation. A decade later, they were re-investigated by Uginčius *et al* [14] within an exact relativistic phase shift analysis based on the numerical code developed by Yennie *et al* [15] and Rawitscher [16]. A number of analytical models were used for the nuclear potential, most of them relying on the two-parameter Fermi charge distribution [17] or on exponential or Gaussian charge distributions [15]. An interesting discovery was an anomaly in the angular distribution of the Sherman function for 40 MeV electrons when scattered from ^{208}Pb at the backmost angles where *S* has a deep minimum [14]. This anomaly with respect to the smooth energy dependence of the point-nucleus results did not occur for the 'adjacent' collision energies of 20 and 100 MeV considered in that paper.

For two ultrarelativistic collision energies relevant to parity violation experiments, 850 MeV and 3 GeV, there also exist theoretical predictions for the angular distribution of the Sherman function (including 200 MeV as a test case). Using an extremely refined partial-wave code, Cooper and Horowitz [18] could identify diffraction structures in *S*. Such structures, arising from the finite nuclear charge distribution, had been found earlier in the differential cross section at energies well above 100 MeV (see e.g. [15, 19, 20]). They are the analogon of the Ramsauer structures which appear at collision energies below 1 keV both in elastic [21, 5] and quasi-elastic [22] electron scattering from heavy atoms, and which are due to the presence of the atomic electron cloud. Pilot measurements of *S* in the ultra-relativistic regime (at 200 MeV and beyond 500 MeV) exist for hydrogen and helium targets, but only at angles below 150°, where *S* is small (see e.g. [23–25]). Since such ultrahigh energy experiments are very intricate, the measurement of the spin asymmetry has been restricted to a single angle. There exists no experimental verification of the diffraction structures in *S* yet.

The aim of this work is to bridge the gap between the atomic physics regime (below 15 MeV), where the Sherman function is an established tool to measure the degree of beam polarization [26, 8, 11], and the nuclear physics regime (beyond 200 MeV), where the spin asymmetry is either an unwanted background effect [18] or is used to gain information on intermediate excited nuclear states which play a dominant role at forward angles for energies above 800 MeV [27, 28]. It is intended to study the Sherman function for its own sake, locating extrema and zeros which depend on energy and target species. A large modulus, particularly for heavy targets, suggests its application to the analysis of the polarization of an electron beam in this intermediate energy region. Near the zeros, on the other hand, it will be shown that there is a great sensitivity of the Sherman function to the underlying nuclear model. Restriction is made, however, to the scattering from spherical (spin-zero) nuclei in order to exclude the influence of magnetic multipoles on the differential cross section at backward angles [29, 30].

The paper is organized as follows. An outline of the formalism of elastic potential scattering, using the phase-shift analysis from [31, 32], is given in section 2. Numerical details are deferred to section 3. The onset of the diffraction structures in the energy dependence of *S* is investigated in section 4, where also the influence of changes in the nuclear potential at the backward angles is discussed. The feasibility of measuring the spin asymmetry for ^{208}Pb up to 80 MeV, where the structures can be clearly identified, is analyzed in section 5. Concluding remarks are given in section 6. Atomic units ($\hbar = m = e = 1$) are used unless indicated otherwise.

2. Theory

We consider the elastic scattering of a spin-polarized relativistic electron from a bare spherical nucleus with charge number Z, the center of mass of the nucleus being fixed at the origin. Since we will concentrate on collision energies above 20 MeV and scattering angles beyond $50°$ where screening effects play no role, the description of the target atom by a bare nucleus is no restriction of the generality. A coordinate system is chosen with the z-axis (e_z) along the initial momentum k_i of the electron, and where the scattering plane, spanned by k_i and the final momentum k_f, coincides with the (x, z)-plane. The normal n to the scattering plane, in the direction of $k_i \times k_f$, defines the y-axis (e_y) and $e_y \times k_i$ defines the x-axis (e_x). The initial and final spin polarization vectors of the electron, $\zeta_i = (\zeta_1, \zeta_2, \zeta_3)$ and ζ_f, respectively, are defined with respect to the above axes.

The differential cross section for the scattering of the electron into the solid angle $d\Omega$ can be expressed by [31]

$$\frac{d\sigma}{d\Omega}(\zeta_i, \zeta_f) = |\langle \chi_f | \hat{f}_e(k_i, \theta) | \chi_i \rangle|^2, \tag{2.1}$$

where χ_i and χ_f are the (two-component) initial and final spin eigenstates, respectively, and $\hat{f}_e$ is the relativistic electron scattering operator [32]

$$\hat{f}_e(k_i, \theta) = A + B\, n\sigma, \tag{2.2}$$

with θ being the scattering angle, n the normal introduced above and σ the vector of Pauli spin matrices. The scattering amplitudes A and B can be expanded in terms of the Legendre polynomials and associated Legendre functions, respectively [32, 31],

$$A = \frac{1}{2ik_i} \sum_{l=0}^{\infty} [(l+1)(e^{2i\delta_{-l-1}} - 1) + l(e^{2i\delta_l} - 1)]P_l(\cos\theta),$$

$$B = \frac{1}{2k_i} \sum_{l=1}^{\infty} (e^{2i\delta_{-l-1}} - e^{2i\delta_l})P_l^1(\cos\theta), \tag{2.3}$$

where δ_κ are the phase shifts arising from the electron–nucleus potential.

If the spin polarization of the final electron is not observed, (2.1) has to be summed over the two final spin states. Using $\sum_{\zeta_f} |\chi_f\rangle\langle\chi_f| = 1$, one obtains

$$\frac{d\sigma}{d\Omega}(\zeta_i) = \sum_{\zeta_f} \frac{d\sigma}{d\Omega}(\zeta_i, \zeta_f)$$

$$= |A|^2 + |B|^2 + 2\,\mathrm{Re}\,(AB^*)\, n\, \langle \chi_i | \sigma | \chi_i \rangle. \tag{2.4}$$

The spin matrix element $\langle \chi_i | \sigma | \chi_i \rangle = \zeta_i$ is identified with the initial spin direction of the electron [33]. Introducing the differential cross section for initially unpolarized electrons (corresponding to an average over the initial spin states), $(\frac{d\sigma}{d\Omega})_0 = |A|^2 + |B|^2$, (2.4) can be written in the following way:

$$\frac{d\sigma}{d\Omega}(\zeta_i) = \left(\frac{d\sigma}{d\Omega}\right)_0 (1 + S\, n\zeta_i), \tag{2.5}$$

where the Sherman function S is defined by

$$S = \frac{2\,\mathrm{Re}\,(AB^*)}{|A|^2 + |B|^2}. \tag{2.6}$$

For fixed final spin polarization, the general formula is [32, 31]

$$\frac{d\sigma}{d\Omega}(\boldsymbol{\zeta}_i, \boldsymbol{\zeta}_f) = \frac{1}{2}\left(\frac{d\sigma}{d\Omega}\right)_0 \{1 + S\boldsymbol{n}(\boldsymbol{\zeta}_i + \boldsymbol{\zeta}_f)$$

$$+ S_1\,\boldsymbol{\zeta}_i\boldsymbol{\zeta}_f + (1 - S_1)\,(\boldsymbol{n}\boldsymbol{\zeta}_i)\,(\boldsymbol{n}\boldsymbol{\zeta}_f) + S_2\,\boldsymbol{n}\,(\boldsymbol{\zeta}_i \times \boldsymbol{\zeta}_f)\} \tag{2.7}$$

with the polarization correlations

$$S_1 = \frac{|A|^2 - |B|^2}{|A|^2 + |B|^2} \qquad \text{and} \qquad S_2 = \frac{2\,\text{Im}\,(AB^*)}{|A|^2 + |B|^2}. \tag{2.8}$$

Hence, the scattering amplitudes A and B (or equivalently the real quantities $(\frac{d\sigma}{d\Omega})_0$, S, S_1 and S_2) provide a complete description of the elementary scattering process. We remark that (2.7) differs from the corresponding expression given e.g. in [6] or [14] because in these papers the scattering amplitudes are defined differently (following [5]). The interrelation between the polarization correlations S_1, S_2 and the polarization functions R, L defined in [6, 14] is given by $R = -S_1 \sin\theta + S_2 \cos\theta$ and $L = S_1 \cos\theta + S_2 \sin\theta$. They satisfy $S_1^2 + S_2^2 = R^2 + L^2 = 1 - S^2$ [6].

3. Numerical details

For electron scattering from heavy nuclei ($Z \gtrsim 80$), nuclear size effects come into play when the collision energy exceeds 10 MeV [15, 14, 10]. This can be understood from the fact that for a fixed scattering angle θ, the minimum momentum transfer to the nucleus, $q_{\min} = 2k_i \sin(\theta/2)$, determines the inverse of the electron–nucleus distance which is relevant for the scattering process. For $\theta \approx 180°$, $1/q_{\min}$ falls below the radius of the nucleus when the collision energy $E_{i,\text{kin}} \gtrsim 15$ MeV.

We have used two models for the representation of the nuclear potential, both assuming radial symmetry of the charge density $\varrho(\boldsymbol{r})$. The first is the two-parameter Fermi charge density [17, 14],

$$\varrho(r) = \frac{\varrho_0}{1 + e^{(r-c_0)/a}}, \qquad \int_{\mathbb{R}^3} d\boldsymbol{r}\, \varrho(r) = Z, \tag{3.1}$$

with c_0 being the nuclear size and a the surface diffuseness parameters (tabulated e.g. in [34]). This leads to the target potential

$$V_T(r) = -\int_{\mathbb{R}^3} d\boldsymbol{r}'\, \frac{\varrho(r')}{|\boldsymbol{r} - \boldsymbol{r}'|}$$

$$= -4\pi\left[\frac{1}{r}\int_0^r r'^2 dr'\, \varrho(r') + \int_r^\infty r'dr'\, \varrho(r')\right], \tag{3.2}$$

which is calculated on a given r-grid extending to $r_{\max}$ and interpolated by a cubic spline [35] (typically, $r_{\max} \sim 15$–20 fm). For $r > r_{\max}$, $V_T(r) = -Z/r$ is assumed purely Coulombic.

The second model employs the Fourier–Bessel (FB) expansion [36], tabulated in [34] and investigated in comparison with other models in [37],

$$\varrho(r) = \sum_{k=1}^N a_k\, j_0\left(\frac{k\pi r}{R_0}\right), \quad r \leqslant R_0; \qquad \varrho(r) = 0, \quad r > R_0, \tag{3.3}$$

where j_0 is a spherical Bessel function, R_0 is related to the nuclear radius and $a_k, \ k = 1, ..., N$, are the expansion coefficients obeying the normalization condition given in (3.1). This leads to

$$V_T(r) \ = \ -4\pi \sum_{k=1}^{N} a_k \, \frac{1}{q^2} \left[\frac{\sin qr}{qr} \ - \ (-1)^k \right], \ \ r \leqslant R_0; \tag{3.4}$$

$$V_T(r) \ = \ -\frac{Z}{r}, \ \ \ r > R_0,$$

with $q = k\pi/R_0$.

The phase shifts δ_κ can be decomposed into a short-range part δ_s plus the Coulombic part δ_c, such that

$$e^{2i\delta_\kappa} \ = \ e^{2i\delta_c} \cdot e^{2i\delta_s}. \tag{3.5}$$

The Coulomb phase shifts are given by [32]

$$e^{2i\delta_c} \ = \ \frac{\kappa - i\eta \frac{c^2}{E_i}}{\gamma - i\eta} \, \frac{\Gamma(\gamma + 1 - i\eta)}{\Gamma(\gamma + 1 + i\eta)} \, e^{i\pi(l-\gamma)}, \ \ \ \ \gamma \ = \ \sqrt{\kappa^2 - (Z/c)^2}, \tag{3.6}$$

where $\kappa = -l - 1$ if $j = l + \frac{1}{2}$ and $\kappa = l$ if $j = l - \frac{1}{2}$ in the partial-wave decomposition of the electronic wavefunction. The total scattering energy is denoted by $E_i = E_{i,\text{kin}} + c^2$ and $\eta = ZE_i/(k_i c^2)$ is the Sommerfeld parameter. We follow [35] in expressing the quotient of the gamma functions by the phase factor $e^{2i\varphi_0}$ with $\varphi_0 = -\text{Re}\,(i \ln \Gamma(\gamma + 1 - i\eta))$.

The short-range phase shifts δ_s are calculated from the asymptotic behavior of the exact continuum partial-wave solutions to the radial Dirac equation by means of the Fortran 77 package RADIAL of Salvat *et al* [35]. (The Coulomb phase shifts provided in this package, defined differently from (3.6), were not used in our code.) RADIAL is a highly optimized double-precision program necessary for an accurate determination of the polarization correlations up to several hundred MeV.

The scattering amplitudes A and B are calculated with the help of the convergence acceleration introduced by Yennie *et al* [15] for sums $s = \sum_l a_l^{(0)} P_l(x)$ involving the Legendre polynomials P_l (with $x = \cos\theta$), by introducing the mth ($m = 3$) reduced series

$$(1-x)^m \, s \ = \ \sum_l a_l^{(m)} P_l(x),$$

$$a_l^{(k+1)} \ = \ a_l^{(k)} \ - \ \frac{l+1}{2l+3} \, a_{l+1}^{(k)} \ - \ \frac{l}{2l-1} \, a_{l-1}^{(k)}, \ \ \ k = 0, 1, 2. \tag{3.7}$$

In order to represent B as a series involving the Legendre polynomials, we follow [16] to use the relations [31, appendix B],[38] $P_l^1(x) = -[lxP_l(x) - lP_{l-1}(x)]/\sqrt{1-x^2}$ and $xP_l(x) = [(l+1)P_{l+1}(x) + lP_{l-1}(x)]/(2l+1)$. (Note that the sign convention in [31] for P_l^1, used here, differs from the one in [38].) This gives

$$B \ = \ -\frac{1}{2k_i\sqrt{1-x^2}} \sum_{l=0}^{\infty} \left[(e^{2i\delta_{-l}} - e^{2i\delta_{l-1}}) \, \frac{l(l-1)}{2l-1} \right.$$

$$\left. -(e^{2i\delta_{-l-2}} - e^{2i\delta_{l+1}}) \, \frac{(l+1)(l+2)}{2l+3} \right] P_l(x). \tag{3.8}$$

The Legendre polynomials are calculated recursively from $P_l(x) = [(2l-1)xP_{l-1}(x) - (l-1) P_{l-2}(x)]/l$ which was tested to be accurate at least up to $l_\text{max} = 5000$. Typically, for an accuracy of $\sim 10^{-10}$, $l_\text{max} \sim 200$–1000 is needed. For the backmost angles, $\theta \geqslant 179°$, the accuracy had to be lowered to $\sim 10^{-6}$ to achieve convergence for $l < 5000$. With this the accuracy of S
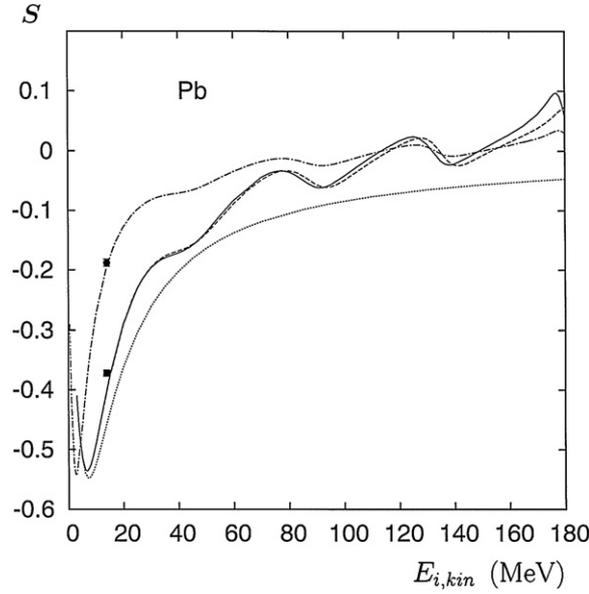
Figure 1. Sherman function S for ^{208}Pb ($Z = 82$) as a function of collision energy $E_{i,\text{kin}}$ at the scattering angle $\theta = 175°$ for the Fourier–Bessel potential ([34] with $N = 13$, see [37], ———), Fermi potential ([14] with $a = 0.5234$, $c_0 = 6.4582$ (in fm), $- - - - -$), as well as for a point nucleus with $Z = 82$ ($\cdots\cdots$). Also shown is the Fourier–Bessel result for $\theta = 168°$ ($- \cdot - \cdot -$). Experimental results at 14 MeV from [10] for $\theta = 168°$ (⬥) and extrapolated to $175°$ (■).

is—even at the largest angles and highest energies considered—better than 1%. In contrast to the Coulomb phase shifts, the short-range phase shifts are already negligible beyond $l = 10$–15 for $E_{i,\text{kin}} \leqslant 200$ MeV.

Our code was tested against the point-nucleus phase shifts, differential cross sections and the Sherman function tabulated in [15, 4, 6]. For an extended nucleus, the code was tested against the differential cross sections and S from [14] and [39]. In all cases, very good agreement with the early calculations was found.

4. Diffraction structures of the Sherman function

For moderate collision energies it is well known that the Sherman function, while being close to zero in the forward hemisphere, has a deep minimum S_{min} at the backward scattering angles. With increasing energy, S_{min} shifts to larger angles θ_{min} ($\theta_{\text{min}} > 170°$ for $E_{i,\text{kin}} > 10$ MeV [6, 14]). Figure 1 displays S as a function of collision energy for a Pb target and the two angles $168°$ and $175°$. For the nuclear potential both variants, (3.2) and (3.4), were used. As compared to the monotone point-nucleus results (i.e. $V_T(r) = -Z/r$ for $r > 0$), oscillations develop for $E_{i,\text{kin}} \gtrsim 40$ MeV which are more pronounced for larger θ. A change in the nuclear potential leads globally to a slight energy shift of the oscillations. These oscillations persist up to infinitely high impact energies because the nuclear potential remains finite at $r = 0$. This is in contrast to the low-energy Ramsauer structures which disappear again when the energy is increased such that the de Broglie wavelength of the impinging electron falls below a fraction of the atom's K-shell radius. (At such energies the scattering is only influenced by the Coulomb field of the nucleus and no longer by the charge cloud of the surrounding
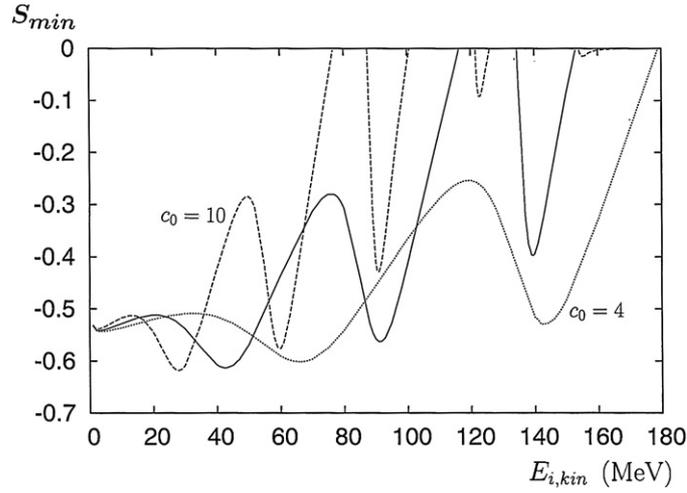
Figure 2. Energy dependence of the backward minimum S_{min} of the Sherman function for $Z = 82$ and a Thomas–Fermi nuclear potential. Parameters $a = 0.5234$ as well as $c_0 = 6.4582$ for ^{208}Pb from [14] (———), $c_0 = 10$ ($---$) and $c_0 = 4$ ($\cdots\cdots$) (in fm).

electrons.) Included in the figure are the experimental results from Sromicki *et al* at 14 MeV [10] which confirm the theory and which clearly show the increase of S due to the finite nuclear size.

A systematic analysis of the minimum of the Sherman function is given in figure 2. For the ^{208}Pb nucleus, it is clearly seen that the anomalously deep minimum of S at 40 MeV, discovered by Uginčius *et al* [14], is in fact close to the minimum value of S_{min} (as a function of $E_{i,kin}$) and marks the onset of the diffraction structures. Even more interestingly, the minimum of the Sherman function ceases to exist near 116 MeV, reappears near 128 MeV and disappears again near 143 MeV in the energy region considered. This behavior is related to the fact of S becoming *positive* (at backward angles) in the respective energy intervals, see figure 1.

In order to study the dependence of the oscillations of S_{min} on the radius of the nucleus (for fixed Z), we have changed the nuclear size parameter c_0 to the fictitious values $\tilde{c} = 4$ (corresponding roughly to the nuclear radius of Zn) and $\tilde{c} = 10$. From figure 2, it becomes clear that the oscillation period scales with the ratio $c_0/\tilde{c}$, and that the oscillations get more intense when the size parameter increases. The energy marking the onset of the oscillations decreases when, $\tilde{c}$ increases, since for a big nucleus a larger de Broglie wavelength of the electron is sufficient to initiate diffractive scattering.

The particular choice of the collision energy near a zero of S_{min} makes the angular distribution of S very sensitive to the choice of the nuclear potential. This is shown for ^{208}Pb in figure 3(a) where S at $E_{i,kin} = 116$ MeV develops a change of sign near $\theta = 120°$ when the Fermi potential is replaced by the Fourier–Bessel potential. In fact, the backward minimum of the former turns into a backward *maximum* in the Fourier–Bessel case.

The variation of the angular dependence of the Sherman function with target species (considering only spin-zero nuclei) is depicted in figures 3(b)–(d) for the two collision energies 80 and 125 MeV. For the heavy nuclei, Pb and U, the diffraction effects become visible near $\theta = 80°$, developing into a deep minimum (beyond 179°) for U at both energies. For Pb, the extremum of S is negative at 80 MeV and positive at 125 MeV (in accordance with figure 2).
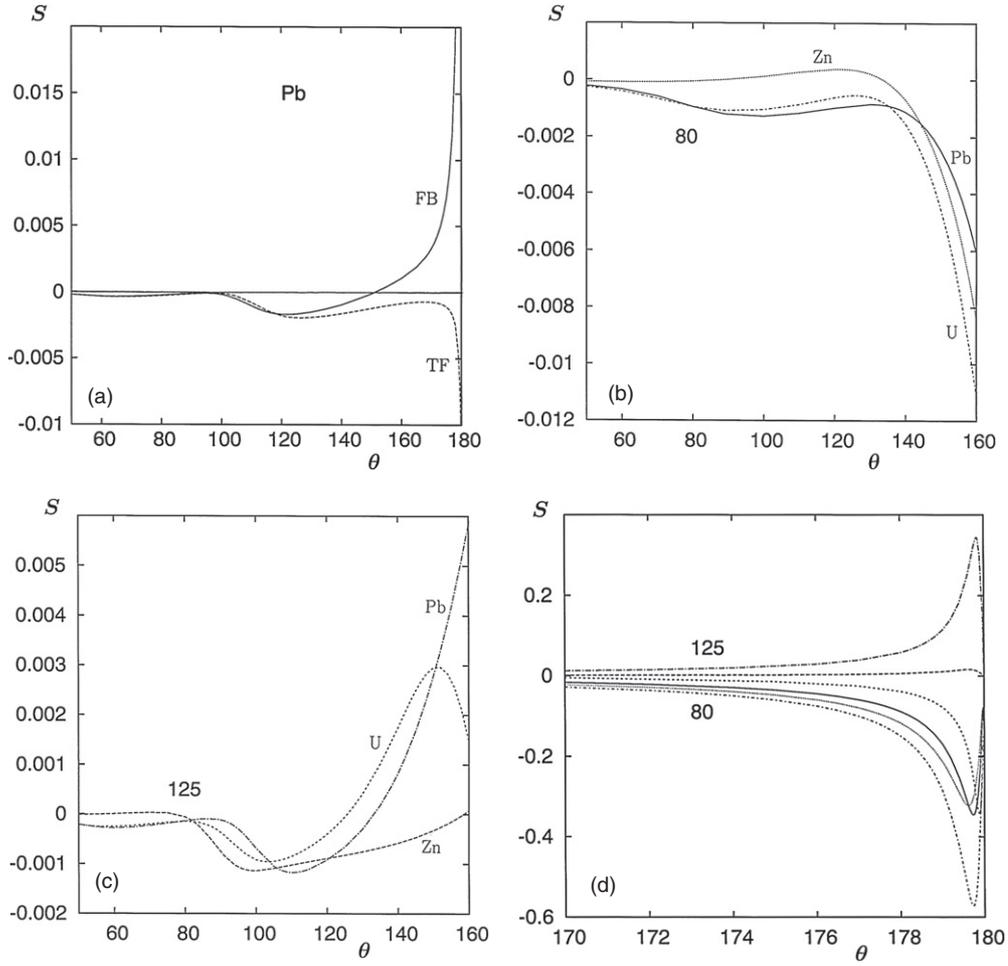
Figure 3. Sherman function S as a function of scattering angle θ:(a) for ^{208}Pb at $E_{i,\mathrm{kin}} = 116$ MeV and the (two-parameter) Fermi potential ($- - --$) compared to the Fourier–Bessel potential (———-). (b) and (d) at $E_{i,\mathrm{kin}} = 80$ MeV for ^{208}Pb (———), ^{64}Zn ($Z = 30$, $\cdots\cdots$) and ^{238}U ($Z = 92$, $- \cdot - \cdot - \cdot -$);(c) and (d) at $E_{i,\mathrm{kin}} = 125$ MeV for ^{208}Pb (— $\cdot$ —- $\cdot$ —), ^{64}Zn (—- —- —) and ^{238}U ($- - --$). For (b)–(d): Fourier–Bessel potential for Zn and Pb; Fermi potential for U ($a = 0.556$, $c_0 = 6.874$ [34]).

For the lighter nucleus, Zn, the structures of S are much weaker. In this case, the first sign change of S occurs near 125 MeV, causing S to be extremely small in the whole backward hemisphere at 125 MeV.

5. Experimental determination of the Sherman function

The theoretically predicted Sherman function can be studied experimentally at several accelerator facilities, like JLAB [24], MAMI [40] or S-DALINAC [41, 42], where electron beams with a degree of polarization $P \sim 80\%$ are routinely available. The polarized electron beam is produced by illumination of a GaAs-type photocathode with circularly polarized laser light. The electrons are accelerated electrostatically to an energy of 100 keV. At MAMI they
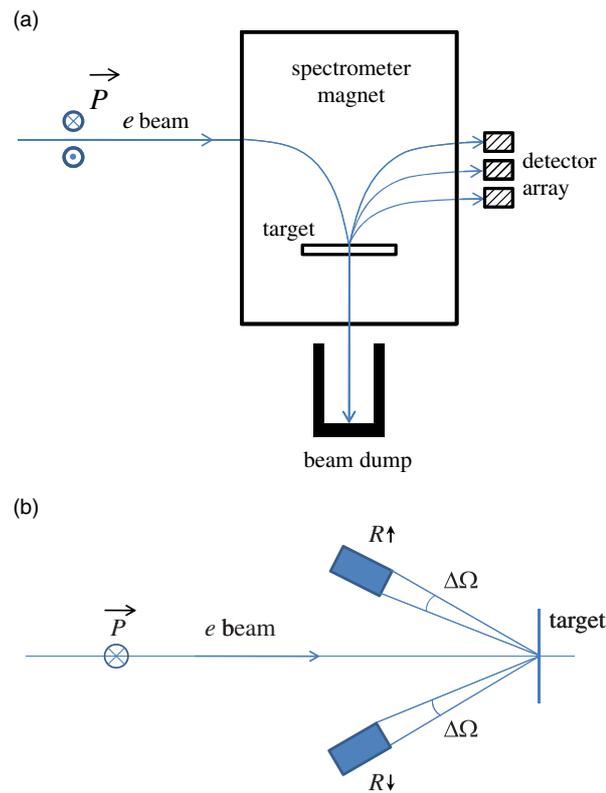
Figure 4. (a) Sketch of the magnetic spectrometer for up–down beam polarization. (b) Schematic view of the Mott scattering geometry for fixed beam polarization.

are then deflected by an α-magnet into the linear accelerator which provides a beam energy around 3.5 MeV where the velocity of light is reached. Using up to three microtron stages, the electrons are further accelerated to their final energy of 1.5 GeV.

The polarized electron guns based on the GaAs-type photocathode deliver a longitudinally polarized electron beam. Since, according to (2.5), the Mott scattering is sensitive to transverse polarization only, a spin manipulator is required. The spin rotation for the Sherman function measurement can be performed with a Wien filter, which consists of crossed homogeneous electric and magnetic fields perpendicular to the beam direction and to each other [43]. The Wien filter is installed between the 100 keV polarized electron source and the injector linac. It can be tuned in such a way that at the position of the target, the beam polarization is strictly perpendicular to the beam direction with an accuracy of $\sim 1°$ [23]. For observation at backward angles, the scattered electrons should be shielded from the primary beam. This can be done with the help of a magnetic spectrometer in order to suppress background radiation, see figure 4(a) [44]. For high-resolution 180° measurements the S-DALINAC is equipped with the powerful QClam spectrometer [45]. In order to measure at several angles simultaneously a movable detector or an array of detectors is favorable.

The asymmetry A in the elastic scattering of the transversely polarized electrons can either be obtained by switching the sign of the electron polarization by means of a fast Pockels cell in the optical system of the polarized electron source, or by placing two detectors on each side of

the beam line as sketched in figure 4(b) (see [11] for more details). Background effects as well as apparative asymmetries can be effectively reduced by a combination of the two methods [10].

The asymmetry is obtained from

$$A = \frac{R \uparrow - R \downarrow}{R \uparrow + R \downarrow},$$ (5.1)

where $R \uparrow$ and $R \downarrow$ are the counting rates in the upper and lower detectors, respectively (or, using the first method, the counting rates corresponding to beams with spin-up and spin-down electrons, respectively). For a complete beam polarization it follows from (2.5) that $S = A$. In a real experimental situation, the Sherman function can be determined by the ratio of the measured asymmetry to the known beam polarization, $S = A/P$. The electron beam polarization can be measured with a standard Mott polarimeter [46, 47] at low incident beam energies or with a Møller polarimeter [48] at high energies.

The expected counting rate R for the detectors can be estimated from the formula

$$R = \left(\frac{d\sigma}{d\Omega}\right)_0 \rho d \frac{N_A}{M} \frac{I_e}{e} \Delta\Omega,$$ (5.2)

where $(\frac{d\sigma}{d\Omega})_0$ is the polarization-averaged differential cross section, $\rho d \frac{N_A}{M}$ is the number of scattering centers per unit area (where ρ is the target density, d is the target thickness, N_A is Avogadro's number and M is the target molecular mass), $\frac{I_e}{e}$ is the number of beam particles per unit time (where I_e is the electron beam current and e is the electron charge) and $\Delta\Omega$ is the detector solid angle.

Introducing the number of counts $N \uparrow \downarrow = R \uparrow \downarrow t_{meas} = R(1 \pm PS) t_{meas}$, an estimate of the error ΔA is obtained from [9]

$$\Delta A = \sqrt{\left(\frac{\partial A}{\partial N \uparrow}\right)^2 (\Delta N \uparrow)^2 + \left(\frac{\partial A}{\partial N \downarrow}\right)^2 (\Delta N \downarrow)^2} = \sqrt{\frac{4 N \uparrow N \downarrow}{(N \uparrow + N \downarrow)^3}},$$ (5.3)

where $\Delta N = \sqrt{N}$ was used. Thus the time interval required for the measurement of the spin asymmetry with a given accuracy $\epsilon = \Delta A/A$ can be estimated by

$$t_{meas} = \left(\frac{A}{\Delta A}\right)^2 \frac{1}{2R} \frac{1 - P^2 S^2}{P^2 S^2} \approx \left(\frac{A}{\Delta A}\right)^2 \frac{1}{2R} \frac{1}{(PS)^2},$$ (5.4)

since in most cases $P^2 S^2 \lesssim 0.1$. From (5.4) with (5.2) it follows that the time required for the experiment is inversely proportional to the quality factor $S^2 \times (\frac{d\sigma}{d\Omega})_0$. Thus, a large spin asymmetry may partially compensate the small cross section at the backward angles. Figure 5 shows the angular dependence of the differential cross section for the two targets ^{208}Pb and ^{64}Zn. At 80 MeV collision energy, the intensity decreases monotonically with θ, with a particularly steep decrease near $180°$ where the Sherman function is largest in modulus. The differential cross section increases with nuclear charge such that a heavy target like Pb or U is also favored in this respect (besides producing larger diffraction structures). While the structures are quite prominent in the angular distribution of S at 125 MeV (see figure 3(c)), they are hardly visible in the differential cross section. This is confirmed by the early relative experimental data from Hofstadter *et al* [49, 19] for ^{208}Pb. For the clear identification of the diffraction structures in the cross section the energy has to exceed 200 MeV (see e.g. [20, 18]).

The behavior of the differential cross section for a ^{208}Pb target with collision energy at fixed angles $\theta \geqslant 160°$ is displayed in figure 6. As compared to the point-nucleus result, the reduction of the cross section is quite formidable; the more so, the higher the energy. This is easily explained because at higher energy the electron gets closer to the center of the nucleus where the difference between the respective (attractive) potentials is infinite. While there are
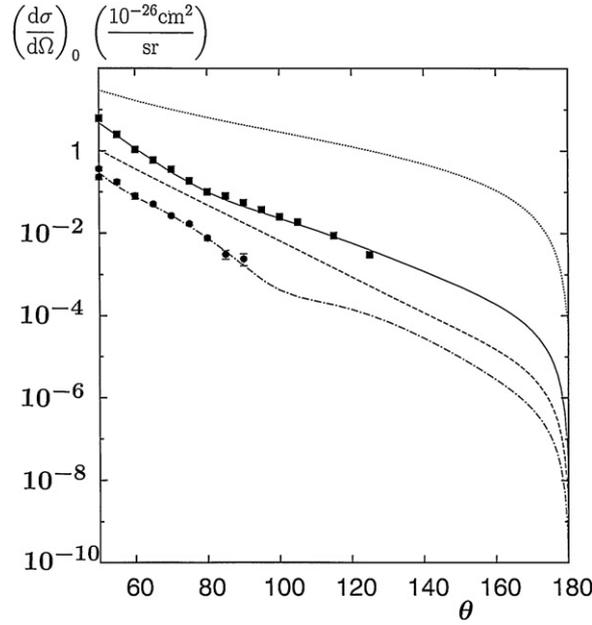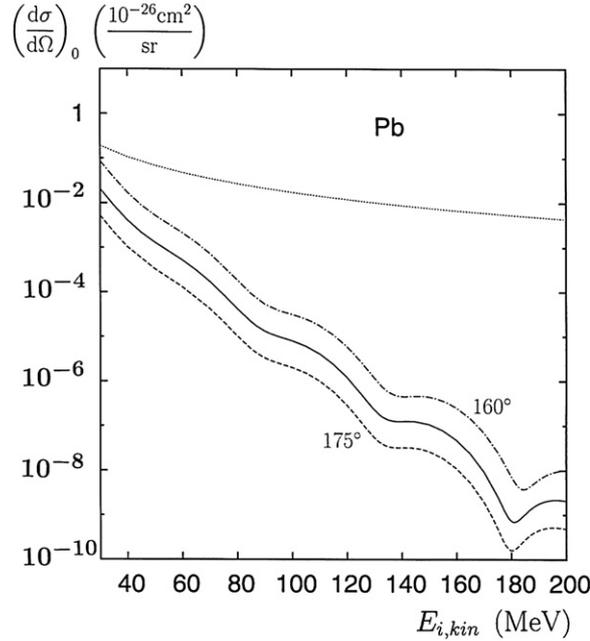
Figure 5. Elastic scattering cross section $(d\sigma/d\Omega)_0$ as a function of scattering angle θ. The beam energy is 80 MeV for ^{64}Zn ($-----$) and ^{208}Pb ($———$), and 125 MeV for ^{208}Pb ($-\cdot-\cdot-$), using the Fourier–Bessel potential. Also shown are point-nucleus ($Z = 82$) results for 80 MeV ($\cdots\cdots$). The experimental data for ^{208}Pb at 84 MeV (■, [19]) and 125 MeV (⧸, [49]) are normalized to theory at $\theta = 80°$.

Table 1. Estimates of the counting rate R and the measurement time t_{meas} for 80 MeV spin-polarized electrons ($P = 0.8$) scattering from a ^{208}Pb target of thickness $d = 15$ μm as a function of angle θ. The beam current is taken $I_e = 100$ μA and the angular acceptance $\Delta\Omega = 10^{-3}$ sr. Only a single scattering is considered.

$E_{i,kin}$(MeV)	θ (°)	ϵ (%)	R (Hz)	t_{meas}(h)
	60	1	3.5×10^5	53
	80	1	3.1×10^4	78
80	160	2.5	57	164
	170	2.5	13	99
	175	2.5	3.2	88
	178	2.5	0.51	86
	179	2.5	0.135	90

no visible structures in the forward hemisphere (in the energy region considered), they appear at the backward angles and are nearly independent of θ beyond 160°. An energy of 80 MeV is favored experimentally for the Pb target because it marks the onset of the diffraction effects (while the intensity is still not too small).

In table 1, we provide estimates for the counting rates as well as for the time required for the measurement, if the accuracy is set to $\epsilon \leqslant 2.5\%$. Such counting rates should be feasible provided the background effects can be sufficiently suppressed in order to provide a good signal-to-noise ratio. Beam currents up to 50 μA for polarized electrons have been achieved at the S-DALINAC [50], and at MAMI, even 200 μA were reached. It should be noted, however, that the quality factor $S^2 \times \left(\frac{d\sigma}{d\Omega}\right)_0$ controls only the statistical uncertainty. When the spin

Figure 6. Elastic scattering cross section $(d\sigma/d\Omega)_0$ as a function of beam energy for ^{208}Pb at $\theta = 160°$ $(- \cdot - \cdot -)$, $170°$ (———), $175°$ $(- - - - -)$, using the Fourier–Bessel potential. Also shown are results for a point nucleus ($Z = 82$) at $170°$ $(\cdots\cdots)$.

asymmetry is smaller than, say, 5×10^{-4}, its precise determination is hampered by additional helicity-dependent factors. Moreover, since multiple scattering in a target of finite thickness will reduce the effective spin asymmetry [10, 11], t_{meas} from table 1 should be considered as a lower bound to the true measurement time.

6. Conclusion

By using an exact partial-wave code for the elastic scattering of polarized electrons from heavy spin-zero target nuclei, we have provided a systematic study of the influence of the nuclear potential on the Sherman function. We have covered the energy region 20–200 MeV where nuclear physics investigations are scarce. The treatment of the nuclei as being inert during the collision is still a reasonable approximation, particularly at the backward scattering angles where the ground-state contribution to the Sherman function is large.

We have found that for heavy targets such as Pb or U, the onset of the diffraction structures occurs near 40 MeV, and that the structures may be identified experimentally at the backward scattering angles when the collision energy is increased to 80 MeV. For this energy, our estimates show that with the presently existing experimental set-ups such a measurement of the Sherman function is feasible at the 3% level.

Whereas it has been common in the atomic physics regime to investigate the angular dependence of S at a given scattering energy, we have directed our interest to the *energy* dependence of S at a fixed backward scattering angle. There, the diffraction-based oscillations show a regular pattern with a nearly constant period. This period scales inversely with the nuclear radius (if the nuclear charge number remains fixed), whereas a change of Z (at fixed radius) merely shifts the oscillations in energy.

In all experiments carried out so far the spin asymmetry was found to be negative in the backward hemisphere. However, the oscillations eventually lead to a periodic sign change of S. Measurements in such regions of near-zero spin asymmetry will be particularly susceptible to the details of the nuclear charge distribution, even more than the diffraction minima in the differential cross section (which begin to appear systematically at energies above 200 MeV). Moreover, for such collision energies the suppression of S in the whole angular regime can be used to design nuclear physics experiments where S is an unwanted background effect.

Acknowledgments

References

[1] Mott N F 1929 *Proc. R. Soc.* A **124** 425
[2] Mott N F 1932 *Proc. R. Soc.* A **135** 429
[3] Shull C G, Chase C T and Myers F E 1943 *Phys. Rev.* **63** 29
[4] Sherman N 1956 *Phys. Rev.* **103** 1601
[5] Mott N F and Massey H S W 1949 *The Theory of Atomic Collisions* 2nd edn (London: Oxford University Press) p 78
[6] Motz J W, Olsen H and Koch H W 1964 *Rev. Mod. Phys.* **36** 881
[7] Kessler J 1969 *Rev. Mod. Phys.* **41** 3
[8] Gellrich A and Kessler J 1991 *Phys. Rev.* A **43** 204
[9] Kessler J 1976 *Polarized Electrons* (Berlin: Springer)
[10] Sromicki J *et al* 1999 *Phys. Rev. Lett.* **82** 57
[11] Tioukine V, Aulenbacher K and Riehn E 2011 *Rev. Sci. Instrum.* **82** 033303
[12] Kerimov B K and Arutyunyan V M 1960 *Sov. Phys.—JETP* **11** 1294
[13] Kresnin A A and Tishchenko B I 1960 *Ukr. Fiz. Zh.* **5** 437
[14] Uginčius P, Überall H and Rawitscher G H 1970 *Nucl. Phys.* A **158** 418
[15] Yennie D R, Ravenhall D G and Wilson R N 1954 *Phys. Rev.* **95** 500
[16] Rawitscher G H 1958 *Phys. Rev.* **112** 1274
[17] Hofstadter R 1957 *Annu. Rev. Nucl. Sci.* **7** 231
[18] Cooper E D and Horowitz C J 2005 *Phys. Rev.* C **72** 034602
[19] Hofstadter R, Hahn B, Knudsen A W and McIntyre J A 1954 *Phys. Rev.* **95** 512
[20] Shevchenko N G *et al* 1967 *Nucl. Phys.* A **101** 187
[21] Ramsauer C 1921 *Ann. Phys., Lpz.* **64** 513
     Ramsauer C 1921 *Ann. Phys., Lpz.* **66** 546
[22] Lucas M W, Jakubassa-Amundsen D H, Kuzel M and Groeneveld K O 1997 *Int. J. Mod. Phys.* A **12** 305
[23] Maas F E *et al* 2005 *Phys. Rev. Lett.* **94** 082001
[24] Armstrong D S *et al* 2007 *Phys. Rev. Lett.* **99** 092301
[25] Heil W *et al* 1989 *Nucl. Phys.* B **327** 1
[26] Gay T J and Dunning F B 1992 *Rev. Sci. Instrum.* **63** 1635
[27] Gorchtein M and Horowitz C J 2008 *Phys. Rev.* C **77** 044606
[28] Afanasev A V 2007 *Proc. WSPC* p 320
[29] Pratt R H, Walecka J D and Griffy T A 1965 *Nucl. Phys.* **64** 677
[30] Rand R E, Frosch R F and Yearian M R 1966 *Phys. Rev.* **144** 859
[31] Joachain C J 1975 *Quantum Collision Theory* (Amsterdam: North-Holland) section 18.3
[32] Berestetskii V B, Lifshitz E M and Pitaevskii L P 1982 *Quantum Electrodynamics (Course of Theoretical Physics* vol 4) 2nd edn (Oxford: Elsevier) sections 37, 80
[33] Tseng H K and Pratt R H 1973 *Phys. Rev.* A **7** 1502
[34] De Vries H, De Jager C W and De Vries C 1987 *At. Data Nucl. Data Tables* **36** 495
[35] Salvat F, Fernández-Varea J M and Williamson W Jr 1995 *Comput. Phys. Commun.* **90** 151
[36] Friar J L and Negele J W 1973 *Nucl. Phys.* A **212** 93
[37] Anni R, Có G and Pellegrino P 1995 *Nucl. Phys.* A **584** 35

[38] Abramowitz M and Stegun I A 1965 *Handbook of Mathematical Functions* (New York: Dover) section 8
[39] Fischer C R and Rawitscher G H 1964 *Phys. Rev.* **135** B 377
[40] Aulenbacher K *et al* 1997 *Nucl. Instrum. Methods* A **391** 498
[41] Richter A 1996 *Proc. EPAC (Sitges, Spain)* p 110
[42] Heßler C *et al* 2008 *Proc. EPAC (Genoa, Italy)* p 1482
[43] Salomaa M *et al* 1977 *Nucl. Instrum. Methods* **145** 279
[44] Aulenbacher K 2011 private communication
[45] Lüttge C *et al* 1995 *Nucl. Instrum. Methods* A **366** 325
[46] Barday R *et al* 2009 *Proc. WSPC* p 105
[47] Steigerwald M 2000 *Proc. SPIN* p 935
[48] Wagner B *et al* 1990 *Nucl. Instrum. Methods* A **294** 541
[49] Hofstadter R, Fechter H R and McIntyre J A 1953 *Phys. Rev.* **92** 978
[50] Eckardt C *et al* 2011 *Proc. Particle Accelerator Conf. (New York)* p 853